ADVANCES IN ATMOSPHERIC SCIENCES, 2024

• **Original Paper** •

Quantifying the Role of the Eddy Transfer Coefficient in Simulating the Response of the Southern Ocean Meridional Overturning Circulation to Enhanced Westerlies in a Coarse-resolution Model

Yiwen LI[1,3], Hailong LIU[*2,3], Pengfei LIN[3], Eric P. CHASSIGNET[4], Zipeng YU[3], and Fanghua WU[5]

[1]*School of Ocean Sciences*, *China University of Geosciences*, *Beijing* 100083, *China*

[2]*Laoshan Laboratory*, *Qingdao* 266237, *China*

[3]*Institute of Atmospheric Physics*, *Chinese Academy of Sciences*, *Beijing* 100029, *China*

[4]*Center for Ocean-Atmospheric Prediction Studies*, *Florida State University*, *Tallahassee* 32306, *Florida*, *USA*

[5]*China Meteorological Administration*, *Beijing* 100081, *China*

(Received 21 October 2023; revised 17 January 2024; accepted 18 February 2024)

ABSTRACT

This study assesses the capability of a coarse-resolution ocean model to replicate the response of the Southern Ocean Meridional Overturning Circulation (MOC) to intensified westerlies, focusing on the role of the eddy transfer coefficient (κ). κ is a parameter commonly used to represent the velocities induced by unresolved eddies. Our findings reveal that a stratification-dependent κ, incorporating spatiotemporal variability, leads to the most robust eddy-induced MOC response, capturing 82% of the reference eddy-resolving simulation. Decomposing the eddy-induced velocity into its vertical variation (VV) and spatial structure (SS) components unveils that the enhanced eddy compensation response primarily stems from an augmented SS term, while the introduced VV term weakens the response. Furthermore, the temporal variability of the stratification-dependent κ emerges as a key factor in enhancing the eddy compensation response to intensified westerlies. The experiment with stratification-dependent κ exhibits a more potent eddy compensation response compared to the constant κ, attributed to the structure of κ and the vertical variation of the density slope. These results underscore the critical role of accurately representing κ in capturing the response of the Southern Ocean MOC and emphasize the significance of the isopycnal slope in modulating the eddy compensation mechanism.

Key words: eddy transfer coefficient, mesoscale eddy parameterization, enhanced westerlies, Southern Ocean Meridional Overturning Circulation, ocean model

Citation: Li, Y. W., H. L. Liu, P. F. Lin, E. Chassignet, Z. P. Yu, and F. H. Wu, 2024: Quantifying the role of the eddy transfer coefficient in simulating the response of the Southern Ocean Meridional Overturning Circulation to enhanced westerlies in a coarse-resolution model. *Adv. Atmos. Sci.*, https://doi.org/10.1007/s00376-024-3278-8.

Article Highlights:

- The eddy compensation response in the Southern Ocean is best captured using a stratification-dependent κ with spatiotemporal variability.
- An enhanced eddy compensation response is driven by the spatial structure term, while the vertical variation term weakens it.
- The temporal variation of κ and the isopycnal slope play key roles in strengthening eddy compensation in the Southern Ocean MOC.

1. Introduction

The Southern Ocean serves as a vital link connecting the Atlantic, Pacific, and Indian Oceans through its meridional overturning circulation (MOC) and the Antarctic Circumpolar Current. Its dynamic nature is influenced by mesoscale eddies, which play a pivotal role in altering volume transport, water mass formation, and carbon absorption within the region (Swart et al., 2014; Waugh, 2014; Gent, 2016). The Southern Ocean MOC comprises two cells: the lower cell and the upper cell. The upper cell involves the upwelling of North Atlantic deep waters and wind-induced northward surface Ekman transport, which is opposite to the

* Corresponding author: Hailong LIU
Email: lhl@lasg.iap.ac.cn

eddy-induced MOC. That is the spatial aspect of the eddy compensation.

Recent observations based on satellite data and atmospheric reanalysis indicate a poleward shift and a 20% intensification of the Southern Hemisphere westerlies due to anthropogenic global warming and stratospheric ozone depletion (Swart and Fyfe, 2012; Bracegirdle et al., 2013; Farneti et al., 2015; Gent, 2016). According to the wind-driven circulation theory, one might expect an enhancement in the Southern Ocean circulations in response to intensified westerlies. However, the isopycnal slope from Argo observations fails to show the anticipated enhancement (Böning et al., 2008). The explanation lies in the phenomenon of the temporal aspect of the eddy compensation within the Southern Ocean.

Eddy compensation occurs as mesoscale eddies absorb energy from the intensified westerlies and, concurrently, are bolstered by this intensification (Viebahn and Eden, 2010; Hofmann and Morales Maqueda, 2011; Downes and Hogg, 2013). Notably, this intricate process of eddy compensation has far-reaching implications. It not only shapes the Southern Ocean's circulation patterns but also significantly influences the sea surface temperature (SST) response to intensified westerlies (Doddridge et al., 2019). The ability to absorb and redistribute energy highlights the importance of eddy compensation in understanding and predicting the state of the Southern Ocean in the context of ongoing climatic shifts.

Most climate models still use non-eddy-resolving ocean models, which means that eddy-induced transport must be parameterized. The eddy parameterization is commonly done using the diffusivity (Redi, 1982) and eddy-induced velocities (Gent and McWilliams, 1990; hereafter referred to as GM), or the skewness flux (Griffies, 1998), with an eddy transfer coefficient (κ). However, GM only parameterizes the transient eddy, so the eddy compensation referred to here is the transient eddy compensation.

To properly parameterize the eddy compensation, κ should be variable in both space and time (Gent, 2016). This has been reported from the analysis of multiple non-eddy-resolving simulations with different ocean models, including the mixing length scheme (Visbeck et al., 1997; Eden and Greatbatch, 2008) and the buoyancy-dependent scheme (Ferreira et al., 2005). Hofmann and Morales Maqueda (2011) showed that the spatiotemporal variation of κ based on the mixing-length scale is important in parameterizing the eddy compensation. Gent and Danabasoglu (2011) emphasized the vertical variation of the buoyancy frequency–dependent κ. Abernathey et al. (2011) found that κ should be proportional to the square root of the wind stress based on a zonal channel model with idealized geometry. While previous studies have indicated the importance of considering both the spatial and temporal variations of κ in simulating the eddy compensation, it is not clear which variation has the greater impact. Additionally, the impact of the additional vertical variation has only been examined using a buoyancy-dependent scheme of κ (Gent and Danabasoglu, 2011). Further investigation with different schemes of κ is necessary to clarify the role of the different characters of κ and the different schemes of κ in the simulation of eddy compensation.

The simulation of eddy compensation in coarse-resolution models requires spatiotemporal variation in κ. However, previous studies have shown inconsistent magnitudes of eddy compensation in response to changes in wind stress. For instance, Hofmann and Morales Maqueda (2011) showed a 67% increase in the eddy-induced MOC with doubled westerlies and a length-scale-dependent scheme for κ, while Gent and Danabasoglu (2011) showed a 60% increase with only 50% enhanced westerlies using a buoyancy-dependent scheme. Furthermore, Downes et al. (2018) found a spread in the simulated trends of the eddy-induced MOC among 12 CORE-II models with different schemes for κ. To understand the spread of eddy compensation in coarse-resolution models, it is necessary to compare the results of different models and schemes. A high-resolution model is usually used as a reference to evaluate the spread, as most state-of-the-art eddy-resolving ocean models can resolve the impact of mesoscale eddies on the MOC response. The idealized channel model by Abernathey et al. (2011) and the eddy-resolving model by Meredith et al. (2012) both indicate a linear response of the eddy-induced MOC to wind stress. Bishop et al. (2016) showed a 22.8% increase in the eddy-induced MOC (transient eddy-induced MOC) with a 50% increase in wind stress using an eddy-resolving coupled model. To determine the crucial features of κ for parameterizing the mesoscale eddies, it is helpful to compare high-resolution with low-resolution configurations of a single model, as this approach avoids the effects of different models' dynamic cores. That evaluation will also help determine the role of spatial and temporal variation of κ in parameterizing the eddy compensation in coarse-resolution models.

This study quantifies the response of the Southern Ocean MOC to increased westerlies in an ocean model that incorporates parameterized eddy effects through different schemes for κ. An eddy-resolving configuration serves as a reference for assessing the effects of different κ on the simulated eddy compensation. Two widely used κ schemes are considered: one depending on the buoyancy frequency from Ferreira et al. (2005), and another that incorporates time and length scales provided by the Eady growth rate, the Rossby radius of deformation, and the Rhines scale from Eden and Greatbatch (2008).

The remainder of the paper is organized as follows. Section 2 describes the ocean model, experiments, and methods of decomposing the eddy-resolving output into the eddy-induced and Eulerian mean transports. In section 3, the response of the circulation to the intensified westerlies in the eddy-resolving model and the coarse-resolution model with different κ schemes are investigated. Section 4 describes how the eddy compensation response in the Southern Ocean is influenced by κ. The last section is a summary

and discussion.

2. Experiments and methods

2.1. *Eddy-resolving experiment*

The ocean model used in this paper was developed at the State Key Laboratory of Numerical Modeling for Atmospheric Sciences and Geophysical Fluid Dynamics (LASG), Institute of Atmospheric Physics (IAP), and named the LASG/IAP Climate system Ocean Model (LICOM). The eddy-resolving experiment uses LICOM version 2.0 (LICOM2.0; Liu et al., 2012), with a 0.1° × 0.1° horizontal grid and 55 vertical levels. In the upper 300 m, 36 levels are used with an average layer thickness of less than 10 m. Biharmonic viscosity and diffusivity schemes are used in the momentum and tracer equations, respectively. The model domain covers 79°S–66°N, excluding the Arctic Ocean. There is a 5° buffer zone at 66°N, where temperature and salinity are restored to the climatological monthly temperature and salinity (Levitus and Boyer, 1994). The experiment, called LICOMH hereafter, was conducted after a 13-year spin-up and using the 60-year (1948–2007) daily Coordinated Ocean-Ice Reference Experiments (CORE; Large and Yeager, 2004) interannually varying forcing. Please refer to Yu et al. (2012) and Liu et al. (2014) for the details of the model description and basic performances.

2.2. *Coarse-resolution experiments*

The coarse-resolution experiments use version 3.0 of LICOM (LICOM3; Li et al., 2020; Lin et al., 2020), which is coupled to the Community Ice Code version 4 (CICE4) through the NCAR flux coupler version 7, with approximately 1° horizontal resolution and 30 vertical levels. The vertical resolution is uniform in the top 150 m, with a grid spacing of 10 m, whereas the spacing is uneven below 150 m. The horizontal model grid uses a tripole grid (Murray, 1996) with two poles in the Northern Hemisphere, which are located at (65°N, 30°W) and (65°N, 150°E), respectively. The tidal mixing parameterization scheme of St. Laurent et al. (2002) is implemented. The coarse-resolution experiments (hereafter referred to as LICOML) follow the second phase of the Coordinated Ocean-Ice Reference Experiments (COREII) protocol, forced by six-hourly atmospheric data and the bulk formula of Large and Yeager (2009). These experiments are integrated for 124 years, with two 62-year CORE-II cycles, and the second cycle is used for analysis here. The strength of the residual MOC, defined as the maximum positive value in the entire area, demonstrates similar trends and variability between the two cycles, except for the first 12 years. The trend of residual MOC from the second cycle is comparable to that from the eddy-resolving experiment, making the comparison between the coarse-resolution simulations and the eddy-resolving simulation valid, despite the skipping of the 12 years at the beginning of the cycle from coarse-resolution experiments and the 13-year spin-up from the eddy-resolving experiment.

There are five coarse-resolution experiments with different schemes for κ (listed in Table 1) to evaluate the influence of κ. The first two experiments, referred to as K500 and K1000, use a constant κ of 500 m^2 s^{-1} and 1000 m^2 s^{-1}, respectively. The next two experiments (called FMH3D and FMH4D, respectively) use a κ scheme based on the structure of buoyancy frequency as described in Ferreira et al. (2005):

$$\kappa = \frac{N^2}{N_{\text{ref}}^2}\kappa_{\text{ref}} , \tag{1}$$

where κ_{ref} is constant and set to 4000 m^2 s^{-1}, N^2 is the buoyancy frequency, and N_{ref}^2 is the reference buoyancy frequency at the bottom of the mixed layer. FMH4D uses a spatiotemporally varying κ, which follows Eq. (1). In FMH3D, its κ is the time-averaged κ during 1948–2009 from FMH4D, making it a control experiment to investigate the impact of the additional temporal variation of κ.

The fifth coarse-resolution experiment, denoted as EG, employs the κ scheme proposed by Eden and Greatbatch (2008), calculated from time and length scales derived from the Eady growth rate, the Rossby radius of deformation, and the Rhines scale:

$$\kappa = \alpha\sigma(x,y,z)L^2(x,y,z) , \tag{2}$$

$$L = \min(L_{\text{r}}, L_{\text{Rhi}}) , \tag{3}$$

$$L_{\text{r}} = \min\left(\frac{c_{\text{r}}}{|f|}, \sqrt{\frac{c_{\text{r}}}{2\beta}}\right) , \tag{4}$$

Table 1. Configurations of the experiments.

Experiment	Resolution (°)	κ (m^2 s^{-1})	Period	Forcing
LICOMH	0.1	-	1949–2007	CORE II
K500	1	500	1948–2009	CORE II
K1000	1	1000	1948–2009	CORE II
FMH3D	1	$\overline{\kappa_{\text{ref}}(N^2/N_{\text{ref}}^2)}$	1948–2009	CORE II
FMH4D	1	$\kappa_{\text{ref}}(N^2/N_{\text{ref}}^2)$	1948–2009	CORE II
EG	1	$\alpha\sigma(x,y,z)L^2(x,y,z)$	1948–2009	CORE II

$$c_r = \int_{-h}^{0} N/\pi \mathrm{d}z \,, \tag{5}$$

$$L_{\mathrm{Rhi}} = \frac{\sigma}{\beta} \,, \tag{6}$$

$$\sigma = \frac{\max(f, \sqrt{2\beta c_r})}{\sqrt{R_i + \gamma}} \,, \tag{7}$$

where L represents the eddy length scale, defined as the minimum of the local Rossby radius of deformation (L_r) and the Rhines scale (L_{Rhi}). L_r is given by Eq. (4), where f is the Coriolis parameter and β is the meridional gradient of f. The parameter c_r in Eq. (4) signifies the first baroclinic Rossby wave speed, calculated by Eq. (5), where N is the buoyancy frequency and h denotes the local water depth. L_{Rhi} is estimated as Eq. (6), where σ denotes an inverse eddy timescale derived from the Eady growth rate, calculated by Eq. (7). The Richardson number (Ri) in Eq. (7) is determined by $\mathrm{Ri} = N^2 \left| \frac{\partial u_h}{\partial z} \right|^{-2}$, where $\left| \frac{\partial u_h}{\partial z} \right|$ represents the absolute value of the vertical shear of the velocity. The constant parameter α, of order one, follows the formulation of Eden and Greatbatch (2008) and Eden et al. (2009).

Despite previous studies indicating that the isopycnal diffusivity is influenced by wind stress (Abernathey and Ferreira, 2015) and the diffusivity coefficient (also known as the Redi coefficient; Abernathey and Marshall, 2013) can impact the Southern Ocean MOC in ocean models (Marshall et al., 2017), the focus of this study is solely on investigating the impact of κ (also known as the GM coefficient). In all coarse-resolution experiments, the Redi coefficient is held constant at a value of 500 $\mathrm{m^2\ s^{-1}}$.

2.3. *Decomposition of MOC in LICOMH*

The total MOC, also named the residual MOC, consists of the Eulerian and the eddy-induced MOC. Following Poulsen et al. (2018), the eddy-induced MOC in LICOMH is defined by the deviation of the total MOC from the Eulerian MOC calculated based on time-mean velocities. As in previous studies, we perform the decomposition analysis in the isopycnal coordinate system (e.g., Hallberg and Gnanadesikan, 2006; Munday et al., 2013; Bishop et al., 2016; Poulsen et al., 2018).

The residual MOC over a specified period is given by

$$\psi(y,\sigma)^{\mathrm{High}}_{\mathrm{res}} = -\overline{\int_{\mathrm{west}}^{\mathrm{east}} \int_{z:\rho(x,y,z,t)\leqslant\sigma} v \mathrm{d}z \mathrm{d}x} \,, \tag{8}$$

where $\psi(y,\sigma)^{\mathrm{High}}_{\mathrm{res}}$ is the residual MOC at a given potential density surface σ across a given latitude y; v is the meridional velocity transferred in density coordinates; $\mathrm{d}z$ is the density thickness, which is the product of $\mathrm{d}\rho$ and $\mathrm{d}z/\mathrm{d}\rho$; x, y and z are the usual Cartesian coordinates; and $\rho(x,y,z,t)$ is the potential density, which is calculated with a reference pressure of 2000 dbar. The zonal integration here is from west to east and the potential density layers smaller than the given potential density σ are integrated in the vertical direction. $\bar{()}$ denotes the average operator over time (10 years used here).

To obtain the Eulerian MOC, the decomposition is applied to the monthly velocity over a specified period in density coordinates. As mentioned by Poulsen et al. (2018), the time scale of the monthly outputs is enough to calculate the eddy-induced circulation. First, the velocity is transferred in density coordinates. Then, the time average (10 years used here) is applied to those velocities, resulting in a time-mean field over that period and its monthly deviation. Taking the meridional velocity as an example, we define the decomposition as follows:

$$v(x,y,\rho,t) = \bar{v}(x,y,\rho) + v^*(x,y,\rho,t) \,, \tag{9}$$

where $\bar{v}$ is the time-mean meridional velocity and v^* is the deviation. The streamfunction derived from the time-mean field represents the Eulerian mean overturning circulation over that period, which includes the standing eddy. The formula is given by

$$\psi(y,\sigma)^{\mathrm{High}}_{\mathrm{Euler}} = -\int_{\mathrm{west}}^{\mathrm{east}} \int_{\bar{z}:\overline{\rho(x,y,z,t)}\leqslant\sigma} \bar{v} \mathrm{d}z \mathrm{d}x \tag{10}$$

where $\psi(y,\sigma)^{\mathrm{High}}_{\mathrm{Euler}}$ is the Eulerian MOC at a given potential density surface σ across a given latitude y; $\bar{v}$ is the time-mean velocity in density coordinates over a specified period (10 years); $\mathrm{d}z$ is the product of $\mathrm{d}\rho$ and $\overline{\mathrm{d}z/\mathrm{d}\rho}$; x, y and z are the usual cartesian coordinates; and $\overline{\rho(x,y,z,t)}$ is the time-mean potential density. The zonal integration here is from west to east and the time-mean potential density layers smaller than the given potential density σ are integrated in the vertical direction.

Finally, the difference between the residual MOC (ψ_{res}) and the Eulerian MOC (ψ_{Euler}) is the eddy-induced MOC:

$$\psi(y,\sigma)^{*\mathrm{High}} = \psi(y,\sigma)^{\mathrm{High}}_{\mathrm{res}} - \psi(y,\sigma)^{\mathrm{High}}_{\mathrm{Euler}} \,, \tag{11}$$

which captures the motion that varies on a temporal timescale shorter than the period of the applied time-averaging operator (10 years used here). The eddy-induced MOC here only represents the MOC induced by the transient eddy.

2.4. *Decomposition of MOC in LICOML*

The decomposition of MOCs in coarse-resolution simulations (LICOML) is different from LICOMH since mesoscale eddies are not resolved in LICOML. Although the residual MOCs in LICOMH and LICOML are the same, the eddy-induced MOC in LICOML is calculated based on the parameterized eddy-induced velocity, which is different from the deviation of the time average in LICOMH. For the coarse-resolution simulations, the residual MOC $[\psi(y,\sigma)^{\mathrm{Low}}_{\mathrm{res}}]$ over a specified period, which is the same as that for the eddy-resolving simulation, is calculated based

on the monthly output of the meridional velocity transferred in the density coordinate. The formula is the same as Eq. (4), which is as follows:

$$\psi(y,\sigma)^{\mathrm{Low}}_{\mathrm{res}} = -\overline{\int_{\mathrm{west}}^{\mathrm{east}} \int_{z:\rho(x,y,z,t)\leqslant\sigma} v\,\mathrm{d}z\,\mathrm{d}x}\,, \qquad (12)$$

where $\psi(y,\sigma)^{\mathrm{Low}}_{\mathrm{res}}$ is the residual MOC for low-resolution simulations at a given potential density surface σ across a given latitude y; v is the simulated residual meridional velocity transferred in density coordinates; $\mathrm{d}z$ is the thickness of the density layers, which is the product of $\mathrm{d}\rho$ and $\mathrm{d}z/\mathrm{d}\rho$ and a crucial component of the MOC; x, y and z are the usual cartesian coordinates; and $\rho(x,y,z,t)$ is the potential density, which is calculated with a reference pressure of 2000 dbar. The zonal integration here is from west to east and the potential density layers smaller than the given potential density σ are integrated in the vertical direction. $\bar{()}$ denotes the average operator over time, which is 10 years here.

However, calculations of the Eulerian MOC and the eddy-induced MOC in LICOML are different from those for LICOMH. The eddy-induced MOC for the coarse-resolution simulation is derived from the monthly parameterized eddy-induced velocity. The formula is as follows:

$$\psi(y,\sigma)^{*\mathrm{Low}} = -\overline{\int_{\mathrm{west}}^{\mathrm{east}} \int_{z:\rho(x,y,z,t)\leqslant\sigma} v^{*}\,\mathrm{d}z\,\mathrm{d}x}\,, \qquad (13)$$

where $\psi(y,\sigma)^{*\mathrm{Low}}$ is the eddy-induced MOC for low-resolution simulations; v^{*} is the parameterized eddy-induced meridional velocity; and x, y, z, $\rho(x,y,z,t)$ and $\mathrm{d}z$ are the same as those in Eq. (7). The zonal integration is also from west to east and the potential density layers smaller than the given potential density σ are integrated in the vertical direction. $\bar{()}$ also denotes the average operator over time, which is 10 years here. Then, the Eulerian MOC for low-resolution simulations is as follows:

$$\psi(y,\sigma)^{\mathrm{Low}}_{\mathrm{Euler}} = \psi(y,\sigma)^{\mathrm{Low}}_{\mathrm{res}} - \psi(y,\sigma)^{*\mathrm{Low}}\,, \qquad (14)$$

where $\psi(y,\sigma)^{\mathrm{Low}}_{\mathrm{Euler}}$ is the Eulerian MOC at a given potential density surface σ across a given latitude y.

3. Responses to enhanced westerlies

3.1. *Enhanced westerlies*

Figure 1a shows the 12-month running mean monthly series of the zonal wind stress averaged in the Southern Ocean (40°–60°S, 0°–360°E) and its linear trend for LICOML. The wind stress was computed using CORE II forcing and model-predicted SST, which indicates an increasing

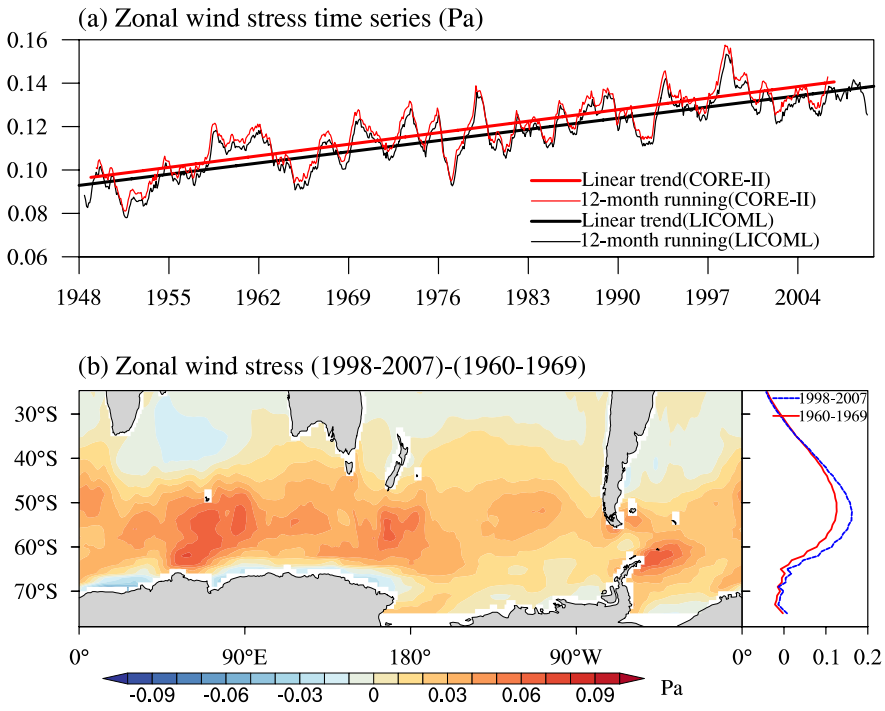

Fig. 1. (a) The 12-month running mean zonal wind stress averaged in the Southern Ocean (40°–60°S and 0°–360°E) from LICOML (thin black line) and the linear trend of the monthly series (thick black line). The red lines are the same as the black lines but for the CORE-II data from 1949 to 2006. (b) Zonal wind stress difference (1998–2007 minus 1960–69) and the zonally averaged values. The red solid and blue dashed lines are for 1960–69 and 1998–2007, respectively.

trend from 1949 to 2007 with a magnitude of about 0.007 Pa (10 yr)$^{-1}$ (significant according to the Mann–Kendall nonparametric test at the significance level of 95%). The trend is consistent with the enhanced westerlies in the Southern Ocean that appeared during recent decades found in CORE II data (Fig. 1a, red lines) and previous studies (Swart and Fyfe, 2012; Bracegirdle et al., 2013; Farneti et al., 2015; Gent, 2016). The difference in the zonal wind stress between 1998–2007 and 1960–69 is presented in Fig. 1b. There is a general enhancement of the zonal wind stress in the Southern Ocean with a mean value of 0.027 Pa and about a 25.2% increase in the strength compared with the first period (0.107 Pa), which is defined by averaging over 40°–60°S and 0°–360°E. Furthermore, a slightly poleward shift of the zonal wind stress is also shown, which is confirmed by previous studies (e.g., Goyal et al., 2021). This significant multidecadal intensification of westerlies in the Southern Ocean is believed to be driven partially by ozone depletion and global warming (Thompson and Solomon, 2002; Marshall, 2003; Miller et al., 2006).

The linear trend of the zonal wind stress in the Southern Ocean from LICOMH is almost the same as that from LICOML with a magnitude of 0.007 Pa (10 yr)$^{-1}$ [Fig. S1 in the electronic supplementary material (ESM)]. For the comparison between the two periods, LICOMH shows an increase in strength of 23.6%, which is 1.6% weaker than the 25.2% from LICOML. That offset comes from both the surface forcing and the feedback from simulated surface speed. The former is mainly due to the mapping process. Therefore, the latter factor may dominate the differences. In addition, the simulated SST may also lead to differences through the calculation of the drag coefficient. However, the zonal wind stress trends in LICOMH and LICOML are almost the same [0.007 Pa (10 yr)$^{-1}$ for both]. Thus, in terms of the response of MOC to intensified westerlies, the difference in the wind stress magnitude between LICOMH and coarse-resolution simulations can be ignored. In general, the enhanced westerlies are well simulated in both LICOML and LICOMH (Fig. S1).

3.2. *Response in the eddy-resolving experiment*

The response of the Southern Ocean MOC to the intensified westerlies is estimated by the eddy-resolving experiment (LICOMH), in which mesoscale eddies can be resolved explicitly. The first row of Fig. 2 shows the residual, Eulerian, and eddy-induced MOC in the isopycnal coordinate system during 1949–2007 in the Southern Ocean. The positive upper cell and the negative lower cell are presented clearly in the residual MOC (Fig. 2a). The upper cell is located from 35°S to 55°S and from 36.05 kg m^{-3} to 36.60 kg m^{-3}. The lower cell is located from 35°S to 75°S and from 36.89 kg m^{-3} to 37.05 kg m^{-3}. This structure is in line with the theoretical pattern in the isopycnal coordinate system (Farneti et al., 2015). The eddy-induced MOC shows the opposite direction to the Eulerian MOC, compensating for the Eulerian MOC and leading to a weaker clockwise residual MOC in the upper cell, which is consistent with previous studies (e.g., Hallberg and Gnanadesikan, 2006; Meredith et al., 2012; Poulsen et al., 2018).

The MOC during 1960–69 and 1998–2007 is presented in the second and third rows of Fig. 2 to evaluate the response of the MOC to enhanced westerlies. To quantify the response, we define the maximal positive value in the whole area as an index to measure the strength of the upper cell, which can represent the total north/south transport in the upper overturning cell at a certain latitude. The clockwise residual MOC during 1998–2007 (Fig. 2g) has a strength of 10.56 Sv, whereas it is 4.73 Sv during 1960–69 (Fig. 2d), indicating a 5.83 Sv increase of the clockwise residual MOC from 1960–69 to 1998–2007. That increase in the strength of the residual MOC (Fig. 2j and Table 2) is 123% compared with that from 1960–69. For the Eulerian MOC in LICOMH, its enhancement is larger than that of the residual MOC, with a strength of 5.84 Sv (Fig. 2k and Table 2), increasing by 59% compared with 1960–69. The ratio of 59% is not in line with the ratio of the enhanced westerlies (25.2%), which may be caused by the changing isopycnal slope (Meredith et al., 2012).

The distinction between the residual and the Eulerian MOC responses can be seen in the compensation effect of the eddy-induced MOC. As illustrated in Fig. 2, the direction of the eddy-induced MOC (Figs. 2c, f, and i) is opposite to that of the Eulerian MOC (Figs. 2b, e, and h) in the region of the upper cell. Additionally, the eddy-induced MOC displays an increase in intensity over time (Fig. 2l). To further quantify this response, the minimum value in the whole area is defined as the strength of the eddy-induced MOC, which can represent the total north/south transport at a certain latitude. The strength is found to be −20.73 Sv during the period 1960–69 and −23.57 Sv during the period 1998–2007. The intensified eddy-induced MOC, referred to as the eddy compensation response, has a strength of 2.84 Sv, constituting 13.7% of the eddy-induced MOC during 1960–69. This ratio is smaller than that of the intensified westerlies (23.6%). This disparity may be caused by the varying isopycnal slope across the Southern Ocean, since the intensified wind stress leads to an increase of a similar magnitude in the overturning with the assumption of a largely invariant isopycnal slope field across the Southern Ocean (Meredith et al., 2012).

Based on the climatological MOCs and their response to changes, there are two categories of eddy compensation. The first category, referred to as simply “eddy compensation”, is the spatial structure of eddy-induced MOC as opposite to that of Eulerian MOC. The second category, referred to as the “response of eddy compensation”, is how the eddy compensation changes as the Eulerian MOC changes due to strengthened westerlies.

3.3. *Responses in the coarse-resolution experiments*

Responses in the coarse-resolution experiments are assessed to evaluate the efficacy of κ. Five different experiments, namely K500, K1000, FMH3D, FMH4D, and EG, each employing a different κ scheme, are examined. The verti-

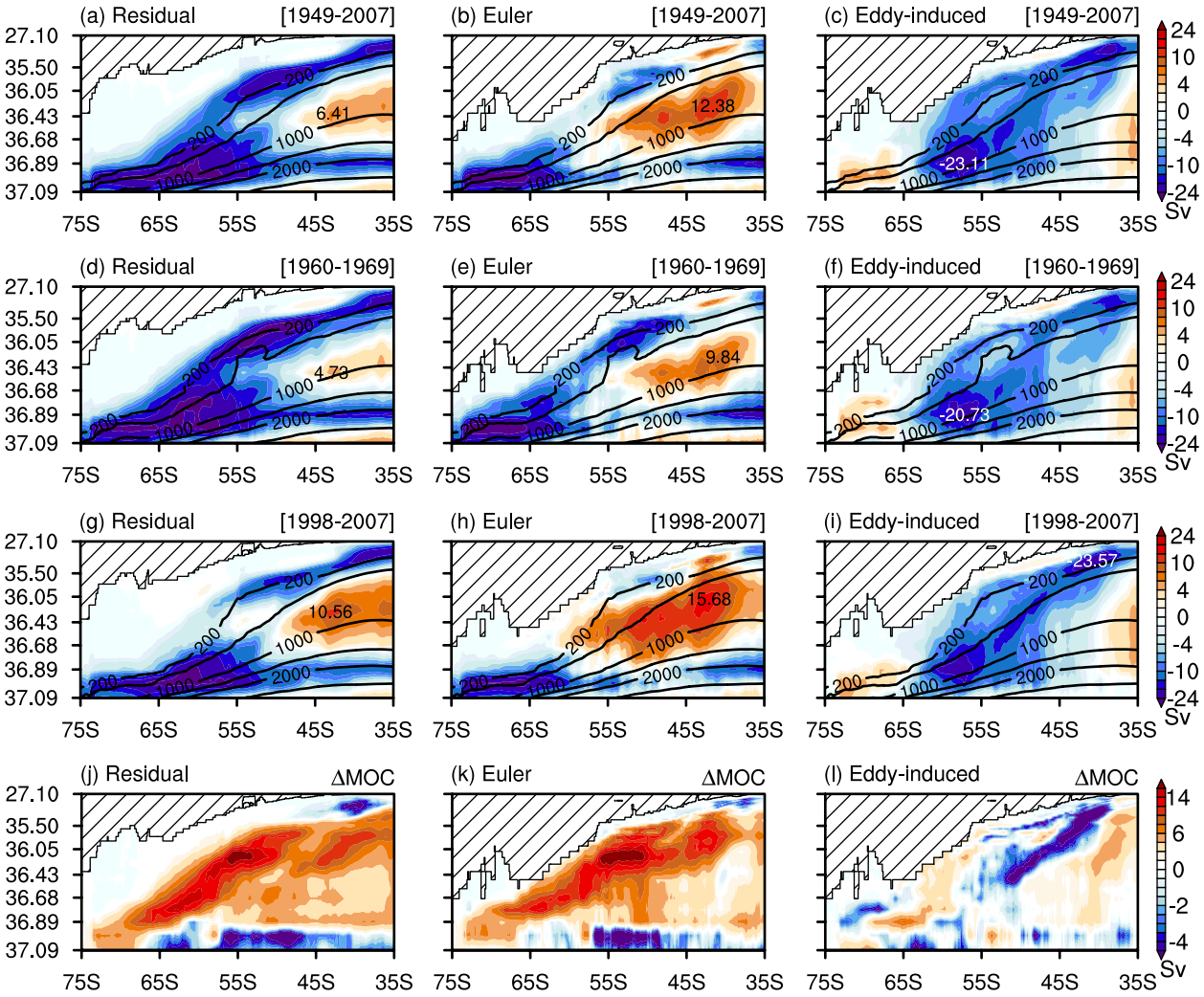

Fig. 2. The residual MOC for the periods (a) 1949–2007, (d) 1960–69, and (g) 1998–2007, and (j) the difference (1998–2007 minus 1960–69), for LICOMH in the isopycnal coordinate. The black curves represent the zonally averaged isobaths (200, 400, 1000, 1500, 2000, and 3000 m) in the isopycnal coordinate. Panels (b, e, h, k) and (c, f, i, l) are the same as (a, d, g, j) but for the Eulerian MOC and eddy-induced MOC, respectively. The *y*-labels in (b, e, h, k) and (c, f, i, l) are exactly the same as in (a, d, g, j). The black numbers in (a, d, g, j) and (b, e, h, k) are the maximums of the closed residual and Eulerian MOC. The white numbers in (c, f, i, l) are the minimums of the eddy-induced MOC. Units: Sv.

Table 2. Differences in the strength for the residual, Eulerian, and eddy-induced MOC between 1960–69 and 1998–2007 for the high-resolution and five coarse-resolution experiments. The strength is the maximal positive value in the whole area for residual and Eulerian MOCs; and for the eddy-induced MOC it is the minimum value in the whole area. Units: Sv.

Experiment	Residual	Eulerian	Eddy
LICOMH	5.83	5.84	−2.84
K500	2.78	2.60	−0.41
K1000	3.19	3.57	−0.36
FMH3D	2.10	6.45	−1.19
FMH4D	1.88	6.54	−2.33
EG	5.35	4.78	−1.68

cal mean κ values for the FMH3D, FMH4D, and EG experiments during the period 1960–69 are displayed in Fig. 3. The K500 and K1000 schemes, which use constant values, are not shown. FMH3D shares a similar spatial pattern to FMH4D, since FMH3D uses the climatological mean κ from FMH4D. Figure 3 reveals distinct spatial patterns: FMH4D exhibits an increasing κ with latitude, while EG shows a decreasing κ with latitude. This discrepancy may arise from the assumption in FMH4D that κ is set as κ_{ref} (4000 m² s^{-1}) in the mixed layer, which is nonadiabatic.

Further investigation is presented in the vertical profiles of κ, displayed in Fig. 4. All three schemes exhibit a decrease in κ with depth, but EG consistently has smaller values across all depths compared to FMH3D and FMH4D. To provide a clearer understanding of the zonal variability and its impact on the zonally averaged values, we have included the zonal mean κ in Fig. 5 (the last column). It illustrates that κ in EG ranges from approximately 200 m^2 s^{-1} to 400 m^2 s^{-1}, except the region shallower than 200 m and

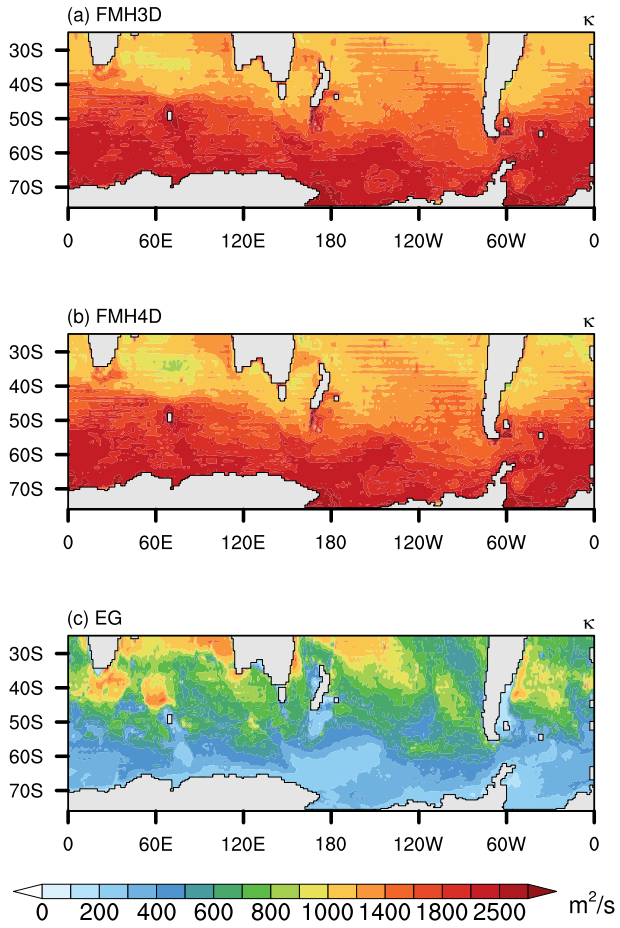

Fig. 3. The vertical mean κ during 1960–69 for (a) FMH3D, (b) FMH4D, and (c) EG. Units: $m^2\ s^{-1}$.

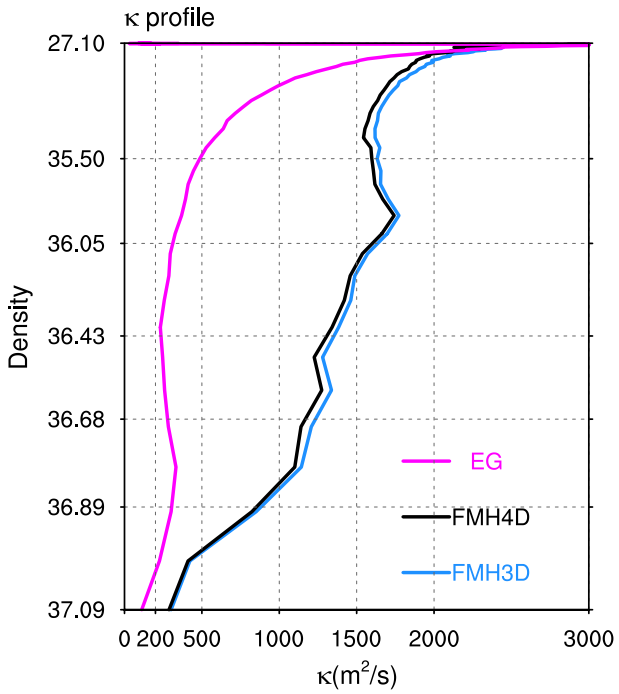

Fig. 4. Vertical profiles of mean κ over the Southern Ocean in FMH3D, FMH4D, and EG during 1960–69. Units: $m^2\ s^{-1}$.

north of 65°S. In contrast, κ values in FMH4D reach 4000 $m^2\ s^{-1}$ in regions shallower than the mixed-layer depth due to the assumption made in FMH4D. Below the mixed-layer depth, the κ values in FMH4D vary depending on the buoyancy, as indicated by Eq. (1). However, there is latitudinal "noise" with a length scale of approximately 2°, which comes from the process of transferring variables from depth coordinates to isopycnal coordinates due to the restricted and coarse vertical resolution of about 0.1 kg m^{-3}. That also causes similar "noise" in the pattern of MOCs.

The impact of the κ schemes on the climatological mean MOCs is investigated. Figure 5 reveals that the climatological mean eddy-induced MOC of all five experiments displays anticlockwise circulations during 1948–2009 (the third column in Fig. 5), which is contrary to the Eulerian MOC (the second column in Fig. 5). Changing the κ value from 500 $m^2\ s^{-1}$ to 1000 $m^2\ s^{-1}$ is expected to result in a stronger eddy-induced MOC (Figs. 5c and g). The patterns of the residual MOC in experiments with spatially varying κ (Figs. 5i, m, and q) show only slight differences compared to K1000, as a result of the compensation between the Eulerian MOC and the eddy-induced MOC. While the climatological residual MOC is barely sensitive to the κ scheme, there are much larger Eulerian and eddy-induced MOC differences between experiments with constant κ and experiments with spatially varying κ. The dependence of the eddy-induced MOC and the Eulerian MOC on the κ scheme may significantly impact the response of the residual MOC to the enhanced westerlies.

Figure 6 shows the responses of the residual, Eulerian, and eddy-induced MOC between 1960–69 and 1998–2007, in which there is a 25.2% enhancement of westerlies in the Southern Ocean. From the first column of Fig. 6, it can be seen that there are obvious differences among the responses of the residual MOC in the five experiments with different κ schemes. Furthermore, the changes in the residual MOC in all five experiments (first column in Fig. 6) are smaller than those of the Eulerian MOC (second column in Fig. 6), which is caused by the compensation of the enhanced anticlockwise eddy-induced MOC (third column in Fig. 6). Thus, the eddy compensation can be simulated with the GM parameterization regardless of the κ scheme. However, compared with the other four experiments, FMH4D has the most extensive enhancement and area of the anticlockwise eddy-induced MOC (third column in Fig. 6) among the five experiments. That largest eddy-induced MOC from FMH4D can reduce its residual MOC, but it is not the smallest, since the Eulerian MOC also plays an important role. The Eulerian MOC also shows sensitivity to κ despite the same change in wind stress. That may be caused by the secondary effects of κ, such as the isopycnal slope (Meredith et al., 2012), which is altered through the eddy-induced transport. Thus, the choice of κ scheme shows the crucial role of κ in simulating the response of the MOC.

To quantify the differences among the five experiments, we also use the defined indexes to measure the strength of the upper cell, which are the maximum value of

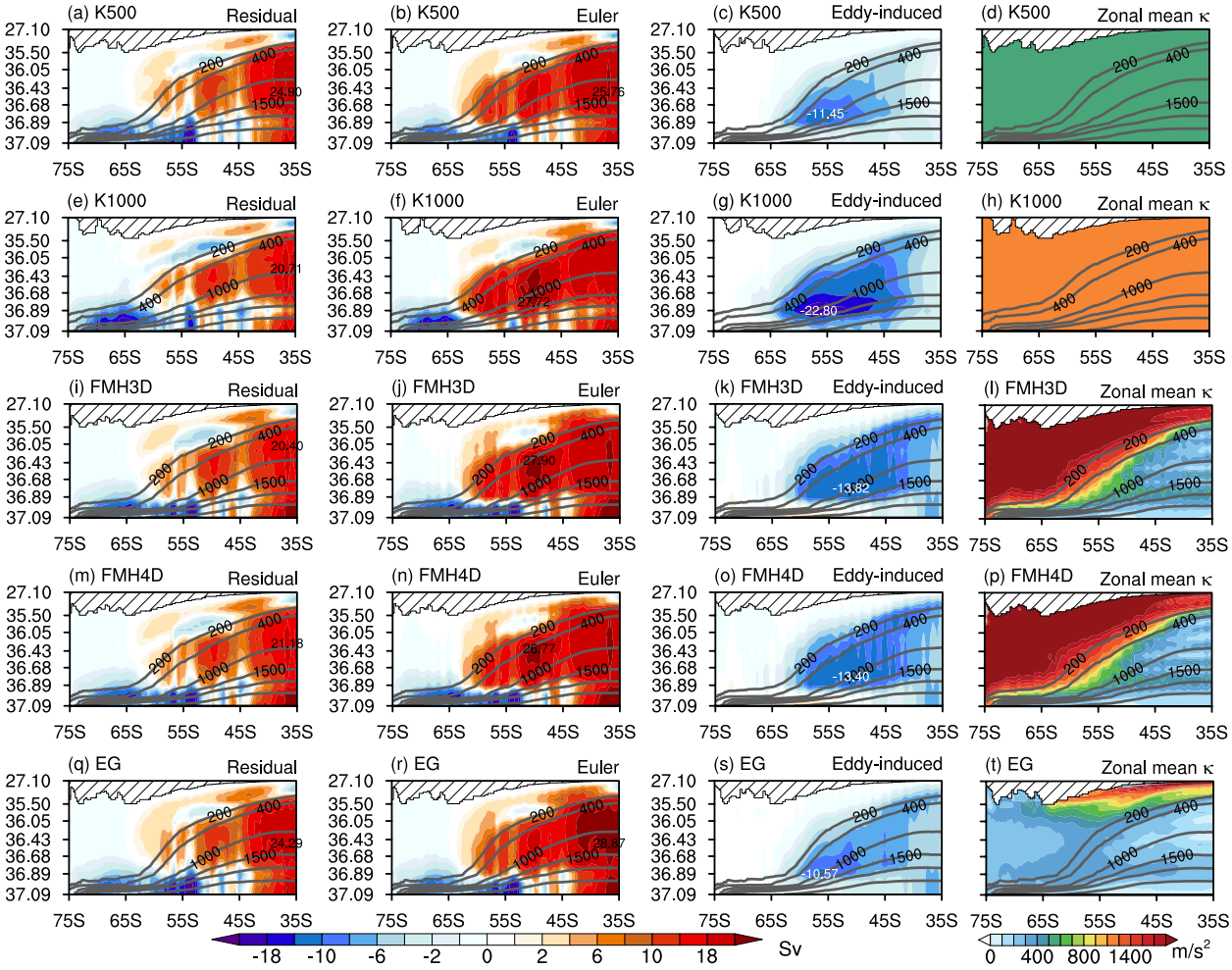

Fig. 5. The (a) residual MOC, (b) Eulerian MOC, (c) eddy-induced MOC, and (d) κ for the K500 experiment during 1948–2009. (e–t) As in (a–d) but for the (e–h) K1000, (i–l) FMH3D, (m–p) FMH4D, and (q–t) EG experiments. The gray lines represent the zonally averaged isobaths (200, 400, 1000, 1500, 2000, and 3000 m) in the isopycnal coordinate system. The black numbers in the first and second columns are the maximum of the residual and Eulerian MOC. The white numbers in the third column are the minimum of the eddy-induced MOC. Units: Sv.

the residual and Eulerian MOC and the minimum value of the eddy-induced MOC in the whole area. The changes in the residual, Eulerian, and eddy-induced MOC between 1960–69 and 1998–2007 are listed in Table 2. The enhanced eddy compensation for LICOMH is −2.84 Sv. For the coarse-resolution experiments, the FMH4D and EG experiments have a relatively larger eddy compensation of −2.33 Sv and −1.68 Sv, respectively, which are closer to LICOMH. For the K500, K1000, and FMH3D experiments, the enhanced eddy-induced MOC is smaller, at −0.41 Sv, −0.36 Sv, and −1.19 Sv, respectively. Thus, the spatiotemporal variance of κ is crucial to the eddy compensation regardless of the κ scheme.

Besides, the comparison between K500 and K1000 suggests that the choice of a constant κ has minimal impact on the eddy compensation response, as the difference between the two values is not statistically significant. The contrast between FMH3D and FMH4D indicates that the spatially varying κ is not sufficient to simulate the full compensation effect. Despite the spatiotemporally varying κ in FMH4D and EG, there is still a nonignorable different eddy compensation response between them. That implies the purely buoyancy-dependent κ leads to a stronger eddy compensation response than the time- and length-scale dependent κ.

Although the eddy compensation response is simulated in all five experiments, the absolute values of the response are all smaller than that in LICOMH. FMH4D has the largest eddy compensation response of −2.33 Sv, which accounts for 82% of LICOMH, whereas K500 only makes up 14% of LICOMH. Therefore, the parameterized eddy with buoyancy-dependent κ can simulate the major eddy compensation response in the eddy-resolving model. The results indicate that the coarse-resolution model fails to capture at least 18% of the eddy compensation response in the high-resolution experiment, suggesting the potential for future improvements in simulating a more comprehensive representation of the eddy compensation response.

Based on the comparison above, we found that the coarse-resolution experiments capture up to 82% of the eddy compensation response from the reference eddy-resolv-

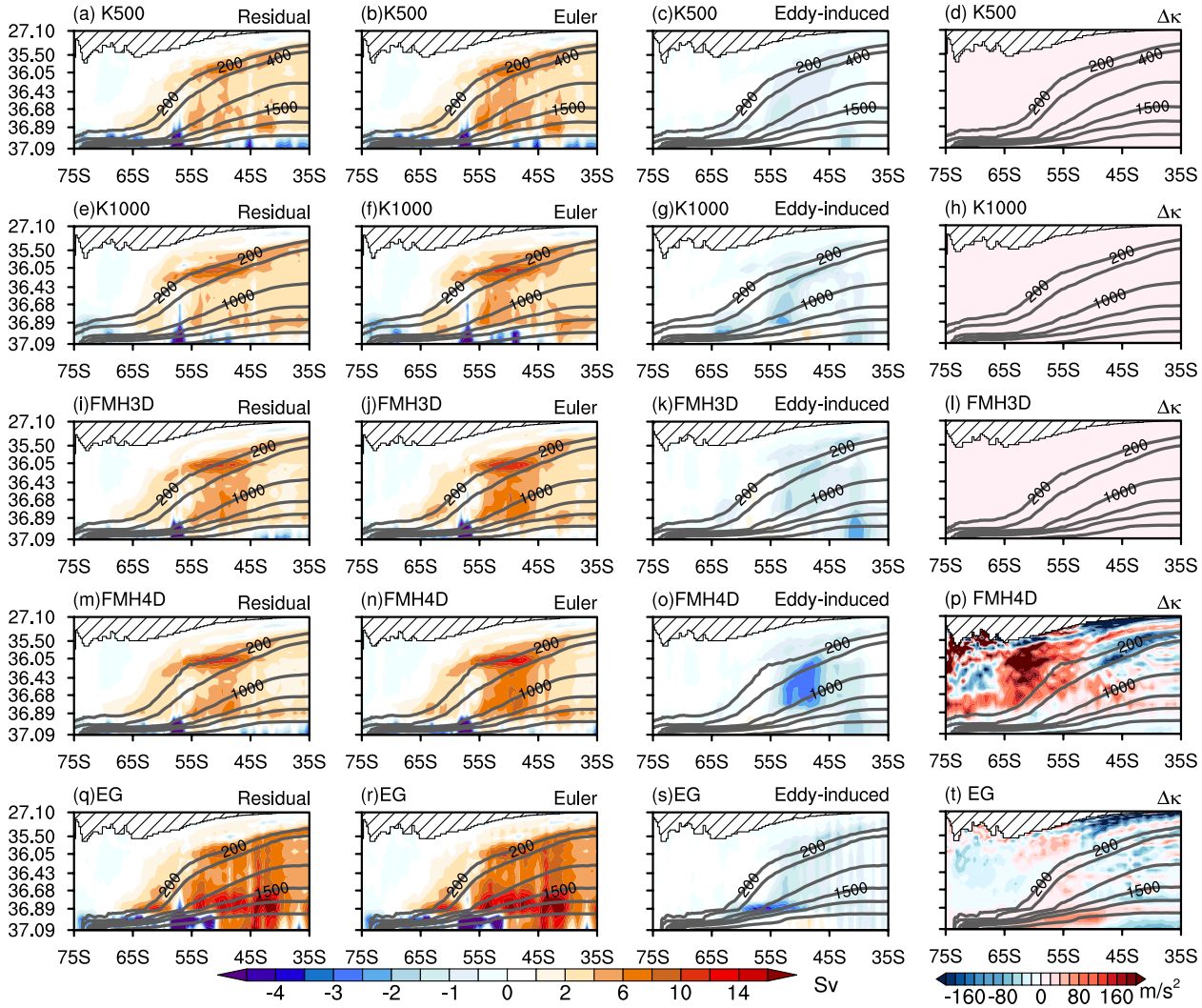

Fig. 6. The (a) residual MOC, (b) Eulerian MOC, (c) eddy-induced MOC, and (d) κ difference (1998–2007 minus 1960–69) ($\Delta\kappa$) for the K500 experiment. The gray lines represent the zonally averaged isobaths (200, 400, 1000, 1500, 2000, and 3000 m) in the isopycnal coordinate system. (e–t) As in (a–d) but for the (e–h) K1000, (i–l) FMH3D, (m–p) FMH4D, and (q–t) EG experiments. Units: Sv.

ing experiment. The spatiotemporal variation of κ based on buoyancy is crucial in simulating the eddy compensation response. This was previously pointed out by Abernathey et al. (2011) through an idealized channel model. Our results indicate that the temporal variation of the buoyancy-dependent κ plays a more significant role in simulating the eddy compensation response than its spatial variation in a global coarse-resolution ocean–sea-ice model. Nevertheless, further analysis is required to understand the effect of the spatiotemporal variation of κ on the eddy compensation.

4. Influence of different κ schemes on the eddy compensation

In this section, we analyze the influence of different κ schemes on the strength of the eddy-induced MOC's enhancement. The eddy-induced velocity in LICOML is parameterized following Gent and McWilliams (1990). The zonal (u^*) and meridional (v^*) eddy-induced velocities can be expressed as functions of κ and the zonal (Slope_x) and meridional (Slope_y) isopycnal slopes:

$$u^* = \left(\kappa \frac{\rho_x}{\rho_z}\right)_z = (\kappa \text{Slope\_}x)_z \,, \tag{15}$$

$$v^* = \left(\kappa \frac{\rho_y}{\rho_z}\right)_z = (\kappa \text{Slope\_}y)_z \,. \tag{16}$$

Here, ρ_x, ρ_y, and ρ_z are the partial differentials of density in the zonal, meridional, and vertical directions, respectively. If κ has vertical variation, the velocity can be decomposed into two terms. The meridional eddy-induced velocity can be presented as

$$v^* = (\kappa \text{Slope\_}y)_z = \kappa(\text{Slope\_}y)_z + \text{Slope\_}y\kappa_z \,, \tag{17}$$

Table 3. Components of the SS and VV terms among the five experiments.

	SS	VV
K500	$\kappa(\text{Slope\_}y)_z$	-
K1000	$\kappa(\text{Slope\_}y)_z$	-
FMH3D	$\kappa(\text{Slope\_}y)_z$	$\kappa_z\text{Slope\_}y$
FMH4D	$\kappa(\text{Slope\_}y)_z$	$\kappa_z\text{Slope\_}y$
EG	$\kappa(\text{Slope\_}y)_z$	$\kappa_z\text{Slope\_}y$

where the two terms on the right-hand side represent the impact of the κ spatial structure (called SS hereafter) and the impact of the vertical variation of κ (called VV hereafter). Those two terms are artificial, which do not have closed streamfunctions. The terms for the five schemes in this study are listed in Table 3. For the experiments with constant κ (K500 and K1000), their eddy-induced velocities only contain the SS part, while experiments with spatially

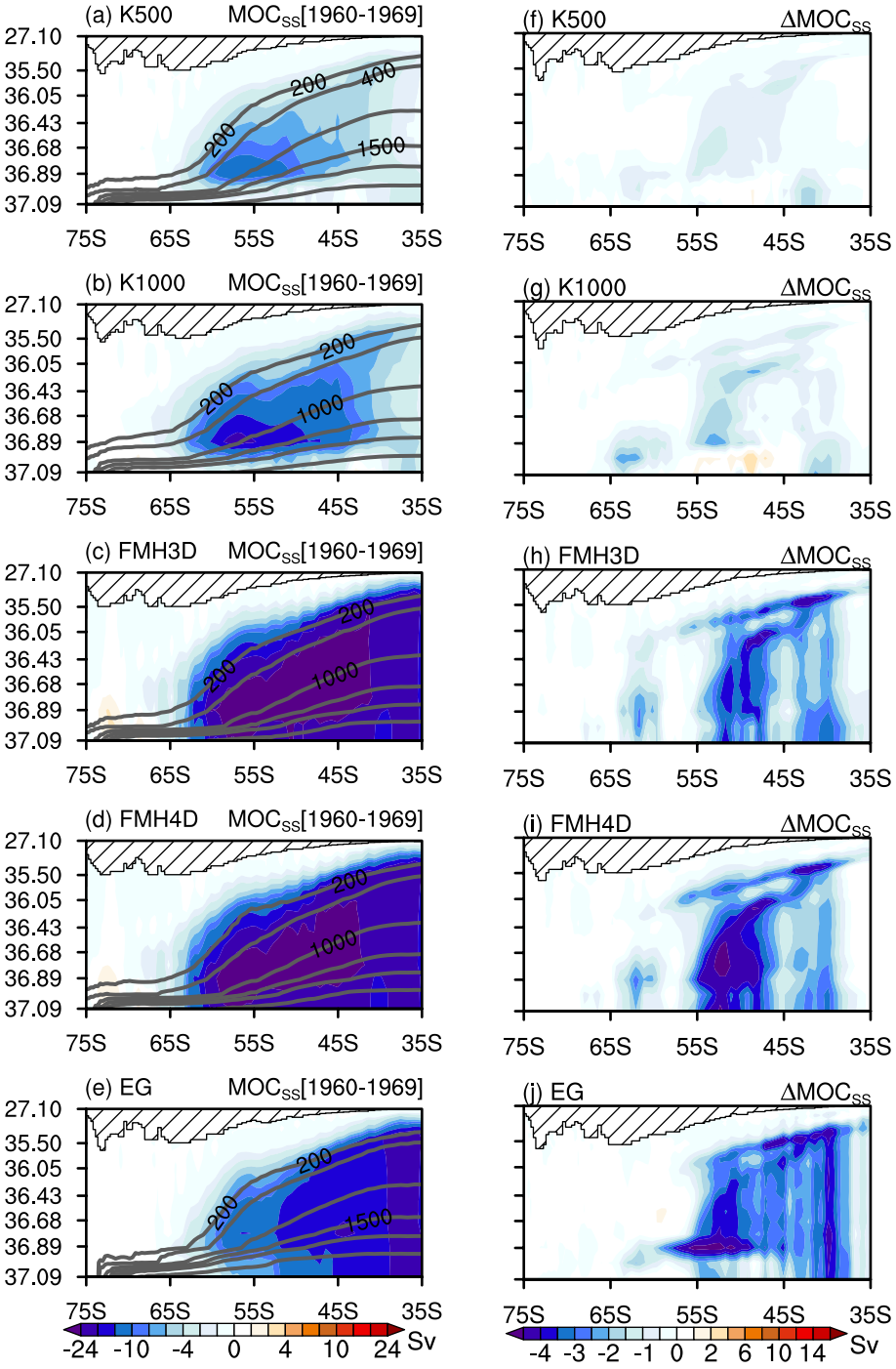

Fig. 7. (a–e) The SS-induced MOC during 1960–69 for (a) K500, (b) K1000, (c) FMH3D, (d) FMH4D, and (e) EG. (f–j) The SS-induced MOC difference (1998–2007 minus 1960–69) for the five experiments. The gray lines in (a–e) are the zonally averaged isobaths (200, 400, 1000, 1500, 2000, and 3000 m) in the isopycnal coordinate system. Units: Sv.

varying κ (FMH3D, FMH4D, and EG) introduce the VV part.

Figure 7 shows the eddy-induced MOC due to the SS term among the five experiments during 1960–69 and the changes between 1960–69 and 1998–2007. The calculation is the same as Eq. (9) but based on the SS-induced velocity. The experiments with constant κ (K500 and K1000) exhibit a closed streamfunction for the SS-induced MOC, while experiments with spatially varying κ show negative values, contributing to eddy compensation. Comparing the experiments, it is evident that spatially varying κ leads to a stronger SS term. Additionally, temporal variation of κ (FMH4D) results in a stronger response of eddy compensation compared to the spatial variation (FMH3D). Although both the FMH4D and EG experiments have larger SS-induced MOC responses than FMH3D, the FMH4D exhibits slightly larger responses than EG.

The SS-induced MOC also exhibits different spatial structures for the different schemes. The constant schemes (K500 and K1000) have MOC centers (10 Sv and 18 Sv) around 55°S and the density surface of 36.89 kg m^{-3}, while FMH3D and FMH4D show centers between 40°S and 60°S and density surfaces of 36.43–36.89 kg m^{-3}, which are larger than 18 Sv. The EG experiment's center is found between 40°S and 75°S and density surfaces of 36.05–36.89 kg m^{-3}. Their responses generally occur between 50°S and 55°S (Figs. 7f and g), which correspond to the latitudes of large wind-stress changes. These differences in the SS-induced MOC structure are reflected in the response of the eddy-induced MOC (Figs. 6c, g, k, o, and s).

Figure 8 shows the VV-induced MOC during 1960–69 for experiments with spatially varying schemes and their responses to enhanced westerlies. The VV-induced MOCs always exhibit a positive or clockwise circulation, compensating for the SS-induced MOCs. However, the changes in the VV-induced MOC are smaller than the changes in the SS-induced MOC. Therefore, the total responses of the eddy-induced MOC are approximately 1 Sv. The dominance of the SS term over the VV term indicates that the eddy compensations in the FMH4D and EG experiments mainly come

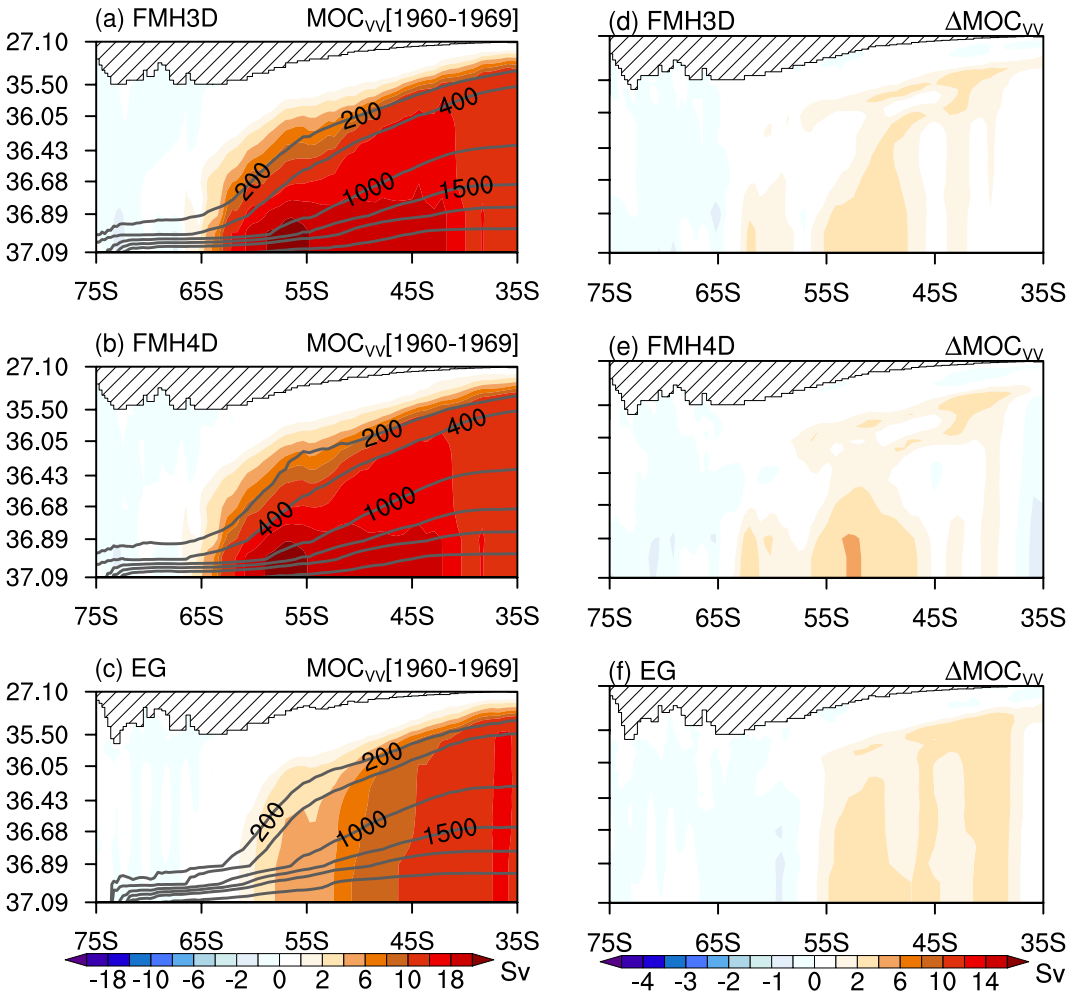

Fig. 8. (a–c) The VV-induced MOC during 1960–69 for (a) FMH3D, (b) FMH4D, and (c) EG. (d–f) The VV-induced MOC difference (1998–2007 minus 1960–69) for (d) FMH3D, (e) FMH4D, and (f) EG. The gray lines in (a–c) are the zonally averaged isobaths (200, 400, 1000, 1500, 2000, and 3000 m) in the isopycnal coordinate system. Units: Sv.

from the enhanced SS-induced MOC rather than the VV-induced MOC resulting from the vertical variation of κ.

The decomposition of the eddy-induced MOC has provided insights into the contribution of different components to eddy compensation. The strongest eddy compensation response in FMH4D can be traced back to the strongest anticlockwise SS-induced MOC response, although the clockwise VV-induced MOC response is non-negligible. Thus, the introduced VV-induced term due to the vertical variation of κ does not enhance the eddy compensation and its response. The stronger eddy compensation and its response in experiments with spatially variant κ can be traced back to the already existing SS-induced term, which is determined by the structure of κ and the vertical variation of the density slope. Besides, the comparison between FMH3D and FMH4D indicates the more important role of temporal variations than that of spatial variations.

In summary, the intensified eddy compensation response is primarily driven by the enhanced SS term, which is intricately influenced by the structure of κ and the vertical variation of the density slope. On the contrary, the introduced VV term due to the vertical variation of κ weakens the response. Additionally, the temporal variation of the stratification-dependent κ plays a key role in strengthening the eddy compensation response to intensified westerlies.

5. Summary and discussion

In this study, we quantified the influence of five κ schemes on the response of the Southern Ocean MOC to intensified westerlies in a non-eddy-resolving ocean model driven by CORE-II forcing. The results indicate that using a buoyancy frequency-based coefficient that varies both spatially and temporally leads to the Southern Ocean MOC response that most resembles the reference response simulated by the eddy-resolving model. However, this parameterization can only replicate 82% of the eddy compensation response in the reference eddy-resolving model.

The study finds that the spatial and temporal variability in buoyancy-dependent κ leads to a six-times-stronger eddy compensation response than a constant κ (5.7 times more than K500 and 6.5 times more than K1000). Despite the importance of the spatial and temporal variations of κ for simulating the eddy compensation response, the temporal variance of κ is more important than its spatial variance, as the eddy compensation response from FMH4D (−2.33 Sv) is two times stronger than that from FMH3D (−1.19 Sv). In addition, the stronger eddy compensation response in the buoyancy-dependent FMH4D scheme (−2.33 Sv) than in the multi-factor-controlled EG scheme (−1.68 Sv) highlights the importance of the buoyancy feature.

A decomposition of the eddy-induced MOC and its response are carried out to investigate the role of the spatial and temporal variation of κ. It indicates that the term derived from the vertical variation of κ does not strengthen the eddy compensation but counteracts it. Those enhanced eddy compensation responses can primarily be attributed to the stronger SS term, which also exists in schemes with constant κ. Hence, the introduction of the spatiotemporal variation of κ does not change the major contribution to the eddy compensation response.

In detail, κ influences the eddy-induced velocity through the GM parameterization initially. Subsequently, the changes in eddy-induced transports of heat and salinity lead to alterations in the global distributions of temperature and salinity, influencing the isopycnal slope. At the same time, the modified surface temperature and salinity impact the heat and freshwater fluxes at the surface, further influencing the temperature, salinity, and overall circulation. These cumulative effects, in turn, affect κ and the eddy-induced velocity, creating a positive feedback cycle.

The results of this study indicate that stratification- and scale-based schemes that allow for spatial and temporal variability in κ improve the simulation of the Southern Ocean MOC's response to climate change. However, it is important to note that the strength of the residual MOC and the Eulerian MOC still show substantial differences between the LICOMH and the five coarse-resolution experiments, which may be due to differences in buoyancy flux and sea-ice coupling (Farneti et al., 2015; Sun et al., 2018). As such, it is necessary to evaluate the eddy compensation in various eddy-resolving models to gain a more realistic reference for coarse-resolution climate ocean models.

Acknowledgements. This study is supported by the National Key R&D Program for Developing Basic Sciences (2022YFC3104802), the National Natural Science Foundation of China (Nos. 42306219 and 42106020) and the Tai Shan Scholar Program (Grant No. tstp20231237). Part of computing resources are financially supported by Laoshan Laboratory (No. LSKJ202300301). Dr. Eric P. CHASSIGNET is supported by the CAS President's International Fellowship Initiative (PIFI) and NOAA Climate Program Office MAPP Program (Award NA15OAR4310088). The data used in this paper can be downloaded from https://osf.io/nr4yf/. Thanks to the editor and the two anonymous reviewers for their suggestions.

Electronic supplementary material: Supplementary material is available in the online version of this article at https://doi.org/10.1007/s00376-024-3278-8.

REFERENCES

Abernathey, R. P., and J. Marshall, 2013: Global surface eddy diffusivities derived from satellite altimetry. *J. Geophys. Res.*, **118**(2), 901–916, https://doi.org/10.1002/jgrc.20066.

Abernathey, R. P., and D. Ferreira, 2015: Southern Ocean isopycnal mixing and ventilation changes driven by winds. *Geophys. Res. Lett.*, **42**, 10 357–10 365, https://doi.org/10.1002/2015GL066238.

Abernathey, R. P., J. Marshall, and D. Ferreira, 2011: The dependence of Southern Ocean meridional overturning on wind stress. *J. Phys. Oceanogr.*, **41**(12), 2261–2278, https://doi.org/10.1175/JPO-D-11-023.1.

Bishop, S. P., P. R. Gent, F. O. Bryan, A. F. Thompson, M. C. Long, and R. Abernathey, 2016: Southern ocean overturning compensation in an eddy-resolving climate simulation. *J. Phys. Oceanogr.*, **46**(5), 1575–1592, https://doi.org/10.1175/JPO-D-15-0177.1.

Böning, C. W., A. Dispert, M. Visbeck, S. R. Rintoul, and F. U. Schwarzkopf, 2008: The response of the Antarctic Circumpolar Current to recent climate change. *Nature Geoscience*, **1**(12), 864–869, https://doi.org/10.1038/ngeo362.

Bracegirdle, T. J., E. Shuckburgh, J.-B. Sallee, Z. M. Wang, A. J. S. Meijers, N. Bruneau, T. Phillips, and L. J. Wilcox, 2013: Assessment of surface winds over the Atlantic, Indian, and Pacific Ocean sectors of the Southern Ocean in CMIP5 models: Historical bias, forcing response, and state dependence. *J. Geophys. Res.*, **118**(2), 547–562, https://doi.org/10.1002/jgrd.50153.

Doddridge, E. W., J. Marshall, H. Song, J.-M. Campin, M. Kelley, and L. Nazarenko, 2019: Eddy compensation dampens Southern Ocean sea surface temperature response to westerly wind trends. *Geophys. Res. Lett.*, **46**, 4365–4377, https://doi.org/10.1029/2019GL082758.

Downes, S. M., and A. M. Hogg, 2013: Southern Ocean circulation and eddy compensation in CMIP5 models. *J. Climate*, **26**(18), 7198–7220, https://doi.org/10.1175/JCLI-D-12-00504.1.

Downes, S. M., P. Spence, and A. M. Hogg, 2018: Understanding variability of the Southern Ocean overturning circulation in CORE-II models. *Ocean Modelling*, **123**, 98–109, https://doi.org/10.1016/j.ocemod.2018.01.005.

Eden, C., and R. J. Greatbatch, 2008: Towards a mesoscale eddy closure. *Ocean Modelling*, **20**(3), 223–239, https://doi.org/10.1016/j.ocemod.2007.09.002.

Eden, C., M. Jochum, and G. Danabasoglu, 2009: Effects of different closures for thickness diffusivity. *Ocean Modelling*, **26**(1–2), 47–59, https://doi.org/10.1016/j.ocemod.2008.08.004.

Farneti, R., and Coauthors, 2015: An assessment of Antarctic Circumpolar Current and Southern Ocean meridional overturning circulation during 1958-2007 in a suite of interannual CORE-II simulations. *Ocean Modelling*, **93**, 84–120, https://doi.org/10.1016/j.ocemod.2015.07.009.

Ferreira, D., J. Marshall, and P. Heimbach, 2005: Estimating eddy stresses by fitting dynamics to observations using a residual-mean ocean circulation model and its adjoint. *J. Phys. Oceanogr.*, **35**(10), 1891–1910, https://doi.org/10.1175/JPO2785.1.

Gent, P. R., 2016: Effects of Southern Hemisphere wind changes on the meridional overturning circulation in ocean models. *Annual Review of Marine Science*, **8**, 79–94, https://doi.org/10.1146/annurev-marine-122414-033929.

Gent, P. R., and J. C. McWilliams, 1990: Isopycnal mixing in ocean circulation models. *J. Phys. Oceanogr.*, **20**(1), 150–155, https://doi.org/10.1175/1520-0485(1990)020<0150:IMIOCM>2.0.CO;2.

Gent, P. R., and G. Danabasoglu, 2011: Response to increasing Southern Hemisphere winds in CCSM4. *J. Climate*, **24**(19), 4992–4998, https://doi.org/10.1175/JCLI-D-10-05011.1.

Goyal, R., A. Sen Gupta, M. Jucker, and M. H. England, 2021: Historical and projected changes in the Southern Hemisphere surface westerlies. *Geophys. Res. Lett.*, **48**, e2020GL090849, https://doi.org/10.1029/2020GL090849.

Griffies, S.M., 1998: The gent–mcwilliams skew flux. *J. Phys. Oceanogr.*, **28**(5), 831-841, https://doi.org/10.1175/1520-0485(1998)028%3C0831:TGMSF%3E2.0.CO;2

Hallberg, R., and A. Gnanadesikan, 2006: The role of eddies in determining the structure and response of the wind-driven Southern Hemisphere overturning: Results from the Modeling Eddies in the Southern Ocean (MESO) project. *J. Phys. Oceanogr.*, **36**(12), 2232–2252, https://doi.org/10.1175/JPO2980.1.

Hofmann, M., and M. A. Morales Maqueda, 2011: The response of Southern Ocean eddies to increased midlatitude westerlies: A non-eddy resolving model study. *Geophys. Res. Lett.*, **38**(3), L03605, https://doi.org/10.1029/2010GL045972.

Large, W. G., and S. G. Yeager, 2004: Diurnal to decadal global forcing for ocean and sea-ice models: The data sets and flux climatologies. NCAR Tech. Note NCAR/TN-460+STR, https://doi.org/10.5065/D6KK98Q6.

Large, W. G., and S. G. Yeager, 2009: The global climatology of an interannually varying air-sea flux data set. *Climate Dyn.*, **33**(2–3), 341–364, https://doi.org/10.1007/s00382-008-0441-3.

Levitus, S., and T. P. Boyer, 1994: World ocean atlas 1994, vol. 4, Temperature. NOAA Atlas NESDIS 4, 129 pp.

Li, Y. W., and Coauthors, 2020: Eddy-resolving simulation of CAS-LICOM3 for phase 2 of the ocean model intercomparison project. *Adv. Atmos. Sci.*, **37**(10), 1067–1080, https://doi.org/10.1007/s00376-020-0057-z.

Lin, P. F., and Coauthors, 2020: LICOM model datasets for the CMIP6 ocean model intercomparison project. *Adv. Atmos. Sci.*, **37**(3), 239–249, https://doi.org/10.1007/s00376-019-9208-5.

Liu, H. L., P. F. Lin, Y. Q. Yu, and X. H. Zhang, 2012: The baseline evaluation of LASG/IAP climate system ocean model (LICOM) version 2. *Acta Meteorologica Sinica*, **26**(3), 318–329, https://doi.org/10.1007/s13351-012-0305-y.

Liu, H. L., Y. Q. Yu, P. F. Lin, and F. C. Wang, 2014: High-resolution LICOM. *Flexible Global Ocean-Atmosphere-Land System Model*, T. J. Zhou et al., Eds., Springer, 321–331, https://doi.org/10.1007/978-3-642-41801-3_38.

Marshall, G. J., 2003: Trends in the Southern Annular Mode from observations and reanalyses. *J. Climate*, **16**(24), 4134–4143, https://doi.org/10.1175/1520-0442(2003)016<4134:TITSAM>2.0.CO;2.

Marshall, J., J. R. Scott, A. Romanou, M. Kelley, and A. Leboissetier, 2017: The dependence of the ocean's MOC on mesoscale eddy diffusivities: A model study. *Ocean Modelling*, **111**, 1–8, https://doi.org/10.1016/j.ocemod.2017.01.001.

Meredith, M. P., A. C. Naveira Garabato, A. M. Hogg, and R. Farneti, 2012: Sensitivity of the overturning circulation in the Southern Ocean to decadal changes in wind forcing. *J. Climate*, **25**(1), 99–110, https://doi.org/10.1175/2011JCLI4204.1.

Miller, R. L., G. A. Schmidt, and D. T. Shindell, 2006: Forced annular variations in the 20th century intergovernmental panel on climate change fourth assessment report models. *J. Geophys. Res.*, **111**(D18), D18101, https://doi.org/10.1029/2005JD006323.

Munday, D. R., H. L. Johnson, and D. P. Marshall, 2013: Eddy saturation of equilibrated circumpolar currents. *J. Phys. Oceanogr.*, **43**(3), 507–532, https://doi.org/10.1175/JPO-D-12-095.1.

Murray, R. J., 1996: Explicit generation of orthogonal grids for

ocean models. *J. Comput. Phys.*, **126**(2), 251–273, https://doi.org/10.1006/jcph.1996.0136.

Poulsen, M. B., M. Jochum, and R. Nuterman, 2018: Parameterized and resolved Southern Ocean eddy compensation. *Ocean Modelling*, **124**, 1–15, https://doi.org/10.1016/j.ocemod.2018.01.008.

Redi, M. H., 1982: Oceanic isopycnal mixing by coordinate rotation. *J. Phys. Oceanogr.*, **12**(10), 1154–1158, 10.1175/1520-0485(1982)012<1154:OIMBCR>2.0.CO;2.

St. Laurent, L. C., H. L. Simmons, and S. R. Jayne, 2002: Estimating tidally driven mixing in the deep ocean. *Geophys. Res. Lett.*, **29**, 2106, https://doi.org/10.1029/2002GL015633.

Sun, S. T., I. Eisenman, and A. L. Stewart, 2018: Does Southern Ocean surface forcing shape the global ocean overturning circulation?. *Geophys. Res. Lett.*, **45**(5), 2413–2423, https://doi.org/10.1002/2017GL076437.

Swart, N. C., and J. C. Fyfe, 2012: Observed and simulated changes in the Southern Hemisphere surface westerly wind-stress. *Geophys. Res. Lett.*, **39**(16), L16711, https://doi.org/10.1029/2012GL052810.

Swart, N. C., J. C. Fyfe, O. A. Saenko, and M. Eby, 2014: Wind-driven changes in the ocean carbon sink. *Biogeosciences*, **11**(21), 6107–6117, https://doi.org/10.5194/bg-11-6107-2014.

Thompson, D. W. J., and S. Solomon, 2002: Interpretation of recent Southern Hemisphere climate change. *Science*, **296**(5569), 895–899, https://doi.org/10.1126/science.1069270.

Viebahn, J., and C. Eden, 2010: Towards the impact of eddies on the response of the Southern Ocean to climate change. *Ocean Modelling*, **34**(3–4), 150–165, https://doi.org/10.1016/j.ocemod.2010.05.005.

Visbeck, M., J. Marshall, T. Haine, and M. Spall, 1997: Specification of eddy transfer coefficients in coarse-resolution ocean circulation models. *J. Phys. Oceanogr.*, **27**(3), 381–402, https://doi.org/10.1175/1520-0485(1997)027<0381:SOETCI>2.0.CO;2.

Waugh, D. W., 2014: Changes in the ventilation of the southern oceans. *Philosophical Transactions of the Royal Society A: Mathematical, Physical and Engineering Sciences*, **372**(2019), 20130269, https://doi.org/10.1098/rsta.2013.0269.

Yu, Y. Q., H. L. Liu, and P. F. Lin, 2012: A quasi-global 1/10° eddy-resolving ocean general circulation model and its preliminary results. *Chinese Science Bulletin*, **57**(30), 3908–3916, https://doi.org/10.1007/s11434-012-5234-8.